Volume and pressure dependences of the electronic, vibrational, and crystal structures of Cs_2CoCl_4: Identification of a pressure-induced piezochromic phase at high pressure

L. Nataf,[1,2] F. Aguado,[1] I. Hernández,[1,3] R. Valiente,[4] J. González,[1] M. N. Sanz-Ortiz,[1,5] H. Wilhelm,[6] A. P. Jephcoat,[6] F. Baudelet,[2] and F. Rodríguez[1,*]

[1]*MALTA TEAM, DCITIMAC, Facultad de Ciencias, University of Cantabria, 39005 Santander, Spain*

[2]*Synchrotron SOLEIL, L'Orme des Merisiers, St. Aubin BP48, 91192 Gif-sur-Yvette, France*

[3]*Materials Research Institute, School of Physics and Astronomy, Queen Mary University of London, Mile End Road, London, E1 4NS, United Kingdom*

[4]*MALTA TEAM, Dpto. Física Aplicada, Universidad de Cantabria-IDIVAL, Spain*

[5]*Bionanoplasmonic Laboratory, CIC biomaGUNE, 2009 Donostia–San Sebastián, Spain*

[6]*Diamond Light Source Ltd., Chilton, Didcot, Oxfordshire, OX11 0DE, United Kingdom*

(Received 25 May 2016; revised manuscript received 28 October 2016; published 24 January 2017)

This work investigates the high-pressure structure of Cs_2CoCl_4 and how it affects the electronic and vibrational properties using optical absorption, Raman spectroscopy, x-ray diffraction, and x-ray absorption in the 0–15 GPa range. In particular, we focus on the electronic and local structures of Co^{2+}, since compression of Cs_2CoCl_4 yields structural transformations associated with change of coordination around Co^{2+}, which are eventually responsible for the intense piezochromism at 7 GPa. This study provides a complete characterization of the electronic and vibrational structures of Cs_2CoCl_4 in the *Pnma* phase as a function of the cell volume and the local $CoCl_4$ bond length, $R_{Co\text{-}Cl}$, as well as its corresponding equation of state. In addition, our interest is to elucidate whether the phase transition undergone by Cs_2CoCl_4 at 7 GPa leads to a perovskite-layer-type structure where Co^{2+} is sixfold coordinated, decomposes into $CsCl + CsCoCl_3$, or it involves an unknown phase with different coordination sites for Co^{2+}. We show that Co^{2+} is sixfold coordinated in the high-pressure phase. The analysis of optical spectra and x-ray diffraction data suggests the formation of an interconnected structure of exchange-coupled Co^{2+} through edge-sharing octahedra at high pressure.

DOI: 10.1103/PhysRevB.95.014110

I. INTRODUCTION

The optical and structural properties of Cs_2CoCl_4 have received considerable attention due to its capabilities as a nonlinear optics material [1–3], ideal quasi-one-dimensional spin-1/2 XY-like antiferromagnet with quantum criticality [4], no pressure shift (0 nm/GPa) of crystal-field-dependent transitions due to covalence effects [5], and the probable existence of a pressure-induced structural phase transition toward higher coordination phases, the nature of which still remains unresolved [6–8]. Besides, the electronic, vibrational, and crystal structures under high-pressure conditions of this relatively compressible compound ($\beta = 0.048\,GPa^{-1}$) allow us to establish structural correlations which are crucial to understand (i) the electronic properties Co^{2+} in tetrahedral coordination in less compressible oxides like ZnO: Co^{2+} [9–12] or $MgAl_2O_4$: Co^{2+} [13–15]; and (ii) how a lattice of independent $CoCl_4$ units evolves under compression toward denser phases involving interconnected $CoCl_4$ tetrahedra and eventually $CoCl_6$ octahedra. The variation of the crystal structure of Cs_2CoCl_4 and Cs_2CuCl_4 under pressure has been previously investigated by x-ray diffraction (XRD) in the 0–5 GPa range using Cs_2CoCl_4 as a compound for exploring the pressure dependence of the Jahn-Teller distorted $CuCl_4$ tetrahedra in Cs_2CuCl_4 [7], which did not show pressure transitions in this range. Although evidences for pressure-induced phase transitions at higher pressures have been reported for Cs_2CoCl_4 through optical absorption [5] and XRD [7], as well as for the isomorphous Rb_2ZnCl_4 by Raman spectroscopy [8,16,17] and XRD [7,8], their high-pressure structure remains unknown. Here we aim to elucidate whether compression of Cs_2CoCl_4 yields layer perovskite-type structures or induces crystal decomposition into cubic CsCl and hexagonal $CsCoCl_3$ with linear chains of interconnected $CoCl_3$ units [18], or different octahedral coordination-based stoichiometric structures (Fig. 1). Unraveling this high-pressure behavior is essential since its optical and magnetic properties strongly depend on the Co^{2+} coordination—the crystal-field strength—and the Co-Co superexchange pathway, i.e., the connection between Co^{2+} ions through Cl^- ligand sharing [4,5,19–21].

Besides its one-dimensional magnetism of exchange-coupled $CoCl_4$ chains along the b axis, Cs_2CoCl_4 exhibits a puzzling optical behavior under pressure associated with the Co^{2+} absorption and with its structural changes [5]. The *d-d* absorption bands, which are responsible for the crystal color, undergo unusual pressure shifts and intensity variations with pressure, showing abrupt changes at 7 GPa. The cyan color exhibited by this crystal between ambient pressure and 7 GPa is produced by the presence of independent $CoCl_4$ tetrahedra in the orthorhombic (*Pnma*) phase [6,22]. The molecular character of $CoCl_4$ in Cs_2CoCl_4 is clearly revealed by Raman spectroscopy through the internal tetrahedron modes at Γ, which also constitutes an efficient probe for local and crystal structures [8,16]. By establishing correlations between the electronic and vibrational structures of Co^{2+} with the local Co-Cl bond length $R_{Co\text{-}Cl}$, through optical absorption, XRD and x-ray absorption (XAS) under pressure, it is possible to determine the bulk and local Grüneisen parameters of the Raman active modes and comparison between local and bulk compressibilities.

*Corresponding author: fernando.rodriguez@unican.es

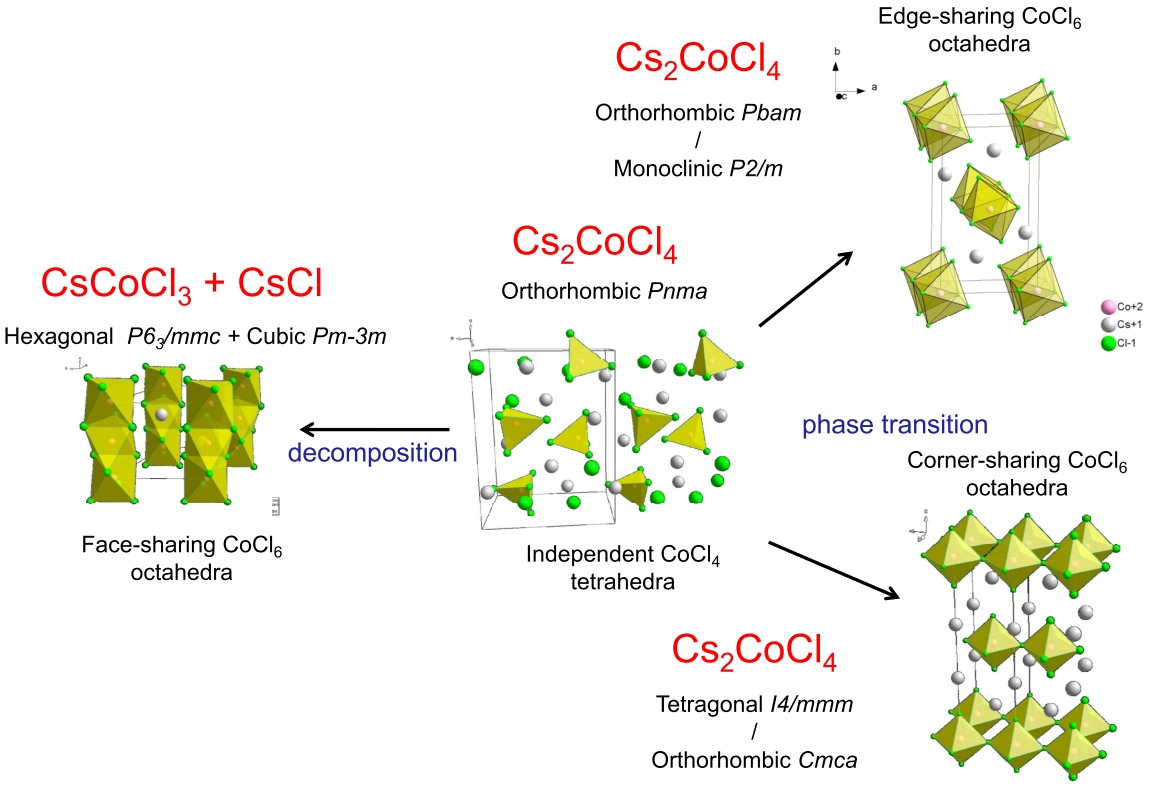

FIG. 1. Orthorhombic *Pnma* crystal structure of Cs_2CoCl_4 at ambient conditions and possible transformation pathways upon compression: (i) decomposition into CsCl plus hexagonal $CsCoCl_3$ $P6_3/mmc$ chain structure, (ii) phase transition to tetragonal $I4/mmm$ or orthorhombic *Cmca* layer perovskite-type structures of corner-sharing octahedra, and (iii) phase transformation involving a denser orthorhombic *Pbam* or monoclinic $P2/m$ structures of edge-sharing octahedra. The coordination of Co^{2+} is indicated by polyhedra in each structure.

II. EXPERIMENTAL

Single crystals of Cs_2CoCl_4 were grown by slow evaporation at 30 °C from acidic (HCl) solution containing a 2:1 stoichiometric ratio of the CsCl and $CoCl_2 \cdot 4H_2O$. The ambient pressure orthorhombic crystal structure, *Pnma* space group (Fig. 1), was checked by XRD on powder samples using a Bruker D8 Advance diffractometer. The measured cell parameters at ambient conditions were $a = 9.720$ Å, $b = 7.313$ Å, and $c = 12.822$ Å.

A membrane diamond anvil cell (MDAC) was used for the high-pressure studies. 200-μm-thick Inconel gaskets were preindented and suitable 300-μm-diameter holes were perforated with a BETSA motorized electrical discharge machine. Given that Cs_2CoCl_4 is soluble in common pressure-transmitting media like methanol-ethanol-water (16:4:1), paraffin and silicone oil were used as alternative pressure transmitting media. These were used to evaluate possible deviations induced by their semihydrostatic or nonhydrostatic behavior in the explored pressure range. It must be noted, however, that according to the ruby line broadening nonhydrostatic effects were not significant in the explored range, as previously reported [23].

The microcrystals used in pressure experiments ($90 \times 70 \times 30 \mu m^3$) were extracted from a Cs_2CoCl_4 single crystal. The Raman spectra were taken with a Horiba T64000 triple spectrometer using the 514.5-nm and 647-nm lines of a Coherent Innova Spectrum 70C Ar^+-Kr^+ laser and a nitrogen-cooled CCD (Jobin-Yvon Symphony) with a confocal microscope. For measuring the low-frequency modes we used the triple monochromator in the subtractive configuration. The experimental setup for room-temperature optical absorption measurements with MDAC has been described elsewhere [24,25]. The detection setup was equipped with a photomultiplier (Hamamatsu R928S) and an InGaAs detector for measurements in the visible and near-infrared range, respectively. The 220-Hz modulated light from a tungsten lamp was dispersed with a 0.5-m single monochromator (Chromex 500IS/SM) equipped with two gratings blazed at 500 and 1100 nm with 1200 and 600 grooves/mm, respectively, and the detected signal was analyzed with a lock-in amplifier (Stanford Research SR830). Pressure was calibrated from the ruby R-line luminescence shift. High-pressure XAS experiments were done at the ODE beamline at the SOLEIL synchrotron. We used a MDAC with perforated diamonds to improve x-ray transmission in the Co K-edge range ($E_K = 7.7$ keV; $\lambda = 1.6$ Å). This was essential to get suitable XAS spectra for extended x-ray absorption fine structure (EXAFS) and x-ray absorption near-edge structure (XANES) analysis in the 10–20 GPa range. Angular dispersion powder XRD experiments were performed at the I15 beam station at the DIAMOND synchrotron using monochromatic wavelength, $\lambda = 0.400$ Å.

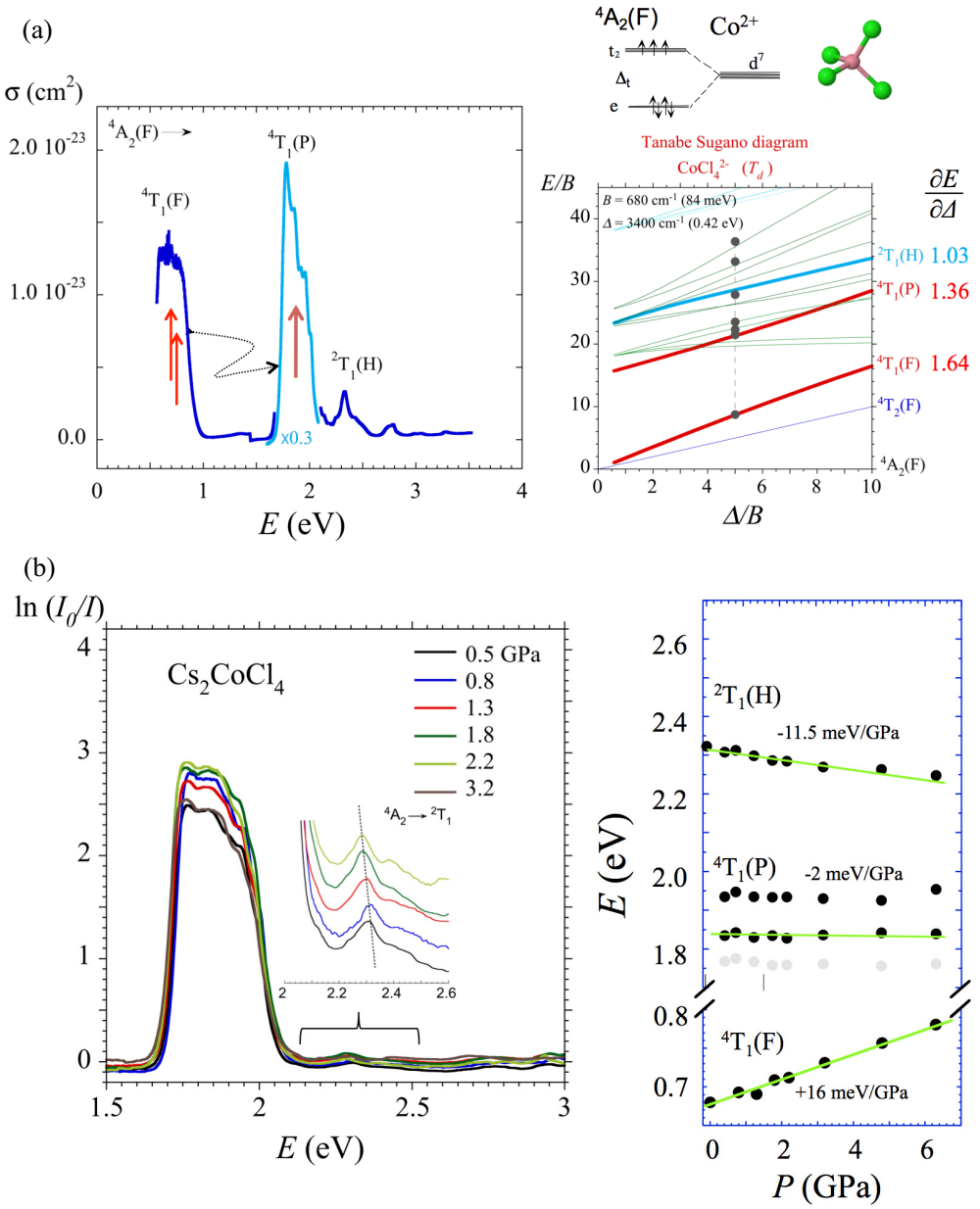

FIG. 2. (a) Absorption spectrum of Cs_2CoCl_4 at ambient conditions. The double red arrow illustrates the excitation of $^4T_1(P)$ state via two-infrared-photon excitation of $^4T_1(F)$ state. The single red arrow indicates one-photon excitation of $^4T_1(P)$. The energies of the main crystal-field transitions are represented in the Tanabe-Sugano diagram for $d^7(T_d)$. The obtained crystal-field parameters at ambient pressure are: $B = 84$ meV and $\Delta_0 = 0.42$ eV with $C/B = 4.4$. Calculated energy derivatives with respect to Δ are given on the right side. (b) Pressure dependence of the absorption spectrum in the orthorhombic *Pnma* phase (0–7 GPa range) is shown on the left side. The energy variation with pressure of the main crystal-field peaks are given on the right side. The corresponding pressure dependences of B and Δ are $\left(\frac{\partial \Delta}{\partial P}\right)_{P_0} = +9.0$ meV/GPa and $\left(\frac{\partial B}{\partial P}\right)_{P_0} = -0.92$ meV/GPa (see text for explanation).

III. RESULTS AND DISCUSSION

A. Optical absorption spectra and piezochromism of Cs_2CoCl_4

Figures 2 and 3 show the optical absorption spectra of Cs_2CoCl_4 as a function of pressure in the *Pnma* phase and along the structural phase transition, respectively, together with the variation of the main absorption bands and their corresponding assignment in terms of Co^{2+} in tetrahedral coordination (*Pnma* phase). Figure 4 shows the peak energy variations as a function of pressure in both *Pnma* and high-pressure phases of Cs_2CoCl_4. The peaks are assigned to tetrahedral or octahedral crystal-field transitions according to the different coordination symmetries around Co^{2+} before and after the phase transition (T_d- or O_h-symmetry notation) [26]. At ambient pressure the spectrum consists of two main spin-allowed transitions from the $^4A_2(F)$ ground state to the $^4T_1(F)$ and $^4T_2(P)$ excited states at 0.68 and 1.84 eV, respectively. The first transition $^4A_2(F) \rightarrow {}^4T_2(F)$ is not observed since it is forbidden by symmetry in T_d. According to the corresponding Tanabe-Sugano (TS) diagram

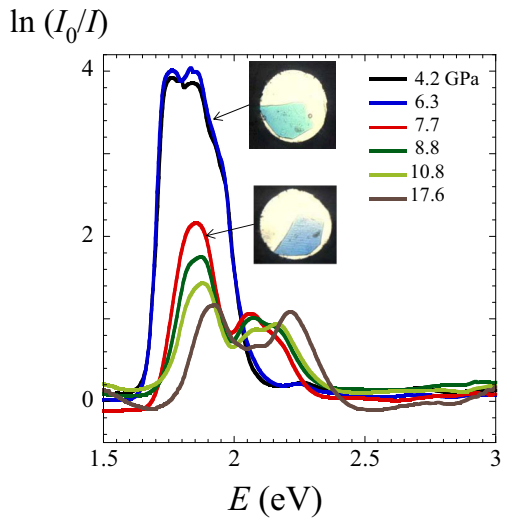

FIG. 3. Variation of the optical absorption spectrum of Cs_2CoCl_4 with pressure showing the piezochromic transformation at 7 GPa. Note the increase of the band splitting and overall absorption reduction above 7 GPa.

(Fig. 2), its energy, which matches the crystal-field splitting (Δ_0), should be at 0.42 eV. Other weak peaks associated with the spin-forbidden transitions ${}^4A_2(F) \rightarrow {}^2T_1(H)$, which are partially activated by the spin-orbit interaction, appear at 2.33 eV. As shown in Fig. 2, the electronic structure of Cs_2CoCl_4 in the *Pnma* phase can be explained through the TS diagrams [26,27], $B = 84$ meV (680 cm^{-1}), $C/B = 4.4$, and $\Delta_0 = 0.42$ eV (3400 cm^{-1}). Note that Δ_0 is about half the crystal-field splitting parameter measured for Co^{2+} in octahedral coordination: $\Delta_0 = 0.86$ eV (6940 cm^{-1}) in $CoCl_2$ [19], as it corresponds to a change in crystal-field strength from $CoCl_4$ (T_d) to $CoCl_6$ (O_h).

The pressure dependence of the transition energies of Co^{2+} in T_d symmetry is represented in Fig. 2. The results are similar to those reported in former high-pressure studies on this compound by Drickamer *et al.* [1,5]. However, in these experiments we have been able to measure the pressure dependence of the additional ${}^2T_1(H)$ weak peak, which is crucial, together with the ${}^4T_1(F)$ and ${}^4T_1(P)$ pressure shifts, for a precise determination of $B(P)$ and $\Delta(P)$.

The ${}^4A_2(F) \rightarrow {}^4T_1(F)$ and the nondetected ${}^4A_2(F) \rightarrow {}^4T_2(F)$ transition energies are both proportional to the crystal-field splitting Δ and therefore shift with pressure towards higher energies provided that Δ increases with pressure. From TS diagrams we obtain that $\left(\frac{\partial E}{\partial P}\right)_{P_0}$ is 1.64 and 1.0 times $\left(\frac{\partial \Delta}{\partial P}\right)_{P_0}$, respectively. However, it must be noted that the Δ-dependent transitions ${}^4A_2(F) \rightarrow {}^4T_1(P)$ and ${}^4A_2(F) \rightarrow {}^2T_1(H)$ shift to lower energies with -2 and -11.5 meV/GPa, respectively, in spite of their transition energy being both proportional to Δ. This effect is a consequence of the pressure-induced reduction of the Racah parameters caused by the increase of the Co-Cl covalency. In the explored pressure range, ${}^4T_1(F)$,${}^4T_1(P)$, and ${}^2T_1(H)$ shift with Δ and B (for $C/B = 4.4$) as $E[{}^4T_1(F)] = 1.64\Delta$; $E[{}^4T_1(P)] = 15.0B + 1.36\Delta$; and $E[{}^2T_1(H)] = 23.2B + 1.03\Delta$. For ${}^4T_1(P)$ and ${}^2T_1(H)$, the competition between two opposite pressure shifts due to the different pressure dependence of B and Δ eventually determines the sign of the effective pressure shift for each transition. From the observed pressure shifts, we obtain linear dependences for both B and Δ as

$$\left(\frac{\partial \Delta}{\partial P}\right)_{P_0} = 9.0 \text{ meV/GPa}, \quad \left(\frac{\partial B}{\partial P}\right)_{P_0} = -0.92 \text{ meV/GPa}.$$

A salient result regarding nonlinear optics concerns the different pressure shift undergone by the ${}^4A_2(F) \rightarrow {}^4T_1(P)$ and ${}^4A_2(F) \rightarrow {}^4T_1(F)$, whose energy is about half of the

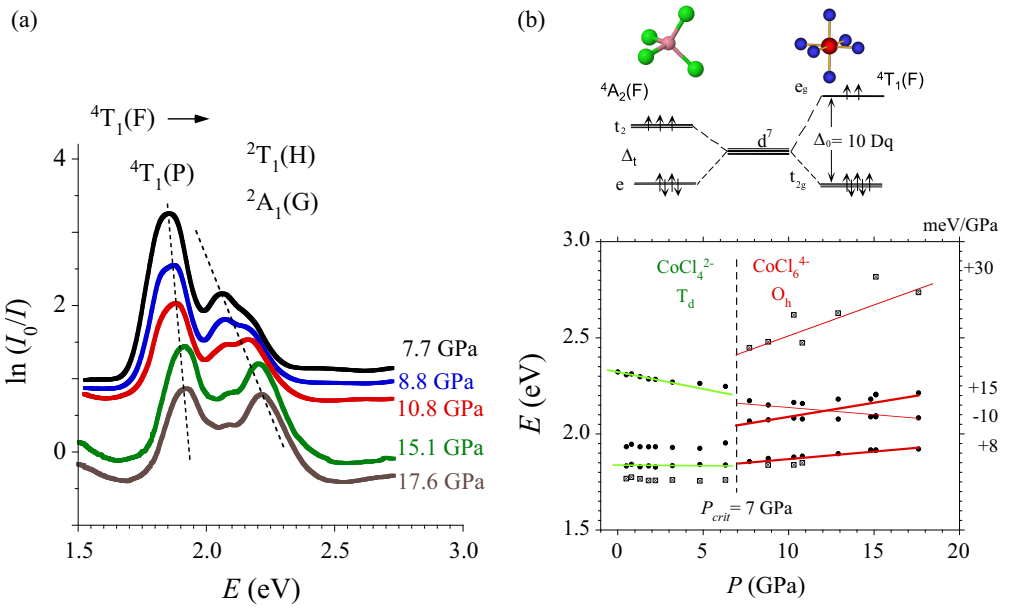

FIG. 4. (a) Variation of the absorption spectrum of Cs_2CoCl_4 as a function of pressure in the high-pressure phase ($P > 7$ GPa). Peak assignment corresponds to Co^{2+} in octahedral coordination following Ref. [31]. (b) Energy variation of the main absorption peaks with pressure in the low- and high-pressure phases. Experimental pressure shift rates are given on the right side.

former (Fig. 2). Present results indicate that ideal conditions for nonlinear effects should be attained at about 10 GPa, where the higher excited state can be resonantly pumped via IR excitation through excited-state absorption processes.

Cs_2CoCl_4 experiences an abrupt transformation at 7 GPa (Fig. 3). Its color changes from cyan to blue and is associated with the absorption decrease in the region of the main band at 1.83 eV. Nevertheless, this decrease is not as much as could be expected if a change of coordination from T_d to O_h occurred at the structural phase transition, as originally suggested by Drickamer *et al.* [1,5]. Instead we detect a complex band structure with at least three noticeable absorption peaks at 1.87, 2.05, and 2.17 eV, the pressure dependence of which is shown in Figs. 3 and 4. The high-pressure optical absorption spectrum is consistent with a sixfold O_h-distorted coordination of Co^{2+} showing an exchange-coupled Co^{2+} connectivity either as a $\cdots Cl_3CoCl_3CoCl_3 \cdots$ linear chain or through $\cdots Cl_4CoCl_2CoCl_4 \cdots$ edge-sharing structures. The presence of strong peaks in the absorption spectra due to nearly centrosymmetric Co^{2+} is ascribed to the spin-effective exchange mechanism [28,29]. This is very efficient for transition-metal ions in concentrated materials such as $CsMnCl_3$ [30], $CsCoCl_3$ [31], or $[(CH_3)_4N]MnCl_3$ [32]. Hence the observed peaks in the Cs_2CoCl_4 high-pressure phase are assigned to crystal-field transitions from the $^4T_1(F)$ ground state (d^7 in O_h) to $^4T_1(P)$ and $^2A_1(G) + {}^2T_1(H)$, the transition oscillator strength of the latter ones being enhanced by the exchange mechanism [31]. A similar transformation was also observed in $[(CH_3)_4N]_2MnCl_4$ and $[(CH_3)_4N]_2MnBr_4$ through time-resolved excitation/emission spectroscopy [32]. Given that these compounds exhibit the same *Pnma* structure for the inorganic/organic tetrahedra at ambient conditions, the absorption spectra of Cs_2CoCl_4 at high pressure suggest a similar structural phase transformation for this compound family upon compression. This structural scenario is supported by Raman spectroscopy, XAS, and XRD measurements.

B. Raman spectroscopy of Cs_2CoCl_4–Pressure effects on the $CoCl_4$ modes

Figures 5 and 6 show the Raman spectrum of Cs_2CoCl_4 at ambient pressure and its variation with pressure in the 0–10 GPa range, respectively. Although there are no previous studies, to the best of our knowledge, on the Raman spectrum of Cs_2CoCl_4 so far to do the assignment, we compare the measured spectrum with those obtained in isomorphous A_2MCl_4 [A : Rb, Cs, $(CH_3)_4N$; M : Zn,Mn,Co] compounds [8,16,17,33–35]. The observed optical phonon peaks correspond to internal modes of the MCl_4^{2-} tetrahedra, and, in the tetramethylammonium-bearing compounds, to internal modes of the organic $(CH_3)_4N^+$ tetrahedra [16,33–35]. Thus, the two peak sets around 130 and 300 cm^{-1} of Cs_2CoCl_4 in its *Pnma* phase (Fig. 5) correspond to the internal vibrations of the $CoCl_4$, according to previous works. In terms of the local T_d symmetry (and D_{2h} crystal symmetry) [16,17], the first set corresponds to the E and T_2 (A_g, B_{1g}, B_{2g}, and B_{3g} in D_{2h}) Cl-Co-Cl bending modes: $\nu_2(E) = 112$ cm^{-1} and $\nu_4(T_2) = 142$ cm^{-1}, whereas the second set corresponds to the A_1 and $T_2(A_{1g}, B_{1g}, B_{2g}$, and $B_{3g})$ Co-Cl stretching modes: $\nu_1(A_1) = 287$ cm^{-1} and $\nu_3(T_2) = 315$ cm^{-1}. Although some

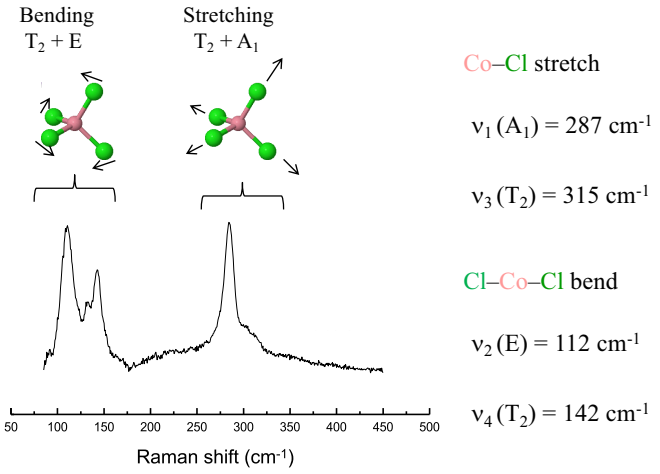

FIG. 5. Raman spectrum of Cs_2CoCl_4 at ambient conditions showing the optical modes corresponding to internal vibrations of the $CoCl_4$ tetrahedron in the orthorhombic *Pnma* phase. Peak assignment in T_d symmetry and corresponding vibrational frequencies are given on the right side.

peaks overlap at ambient pressure, the pressure-induced shifts clarify the peak assignment (Fig. 6). Note that the T_2 modes overlap near ambient pressure but they progressively become better resolved between 3 and 6 GPa, thus indicating that the initially distorted $CoCl_4$ tetrahedron (D_{2d}) as revealed from XRD [7] evolves towards a more regular tetrahedron (T_d) with pressure. The mode frequency increases linearly with pressure for all peaks, at a rate ranging from 5 to 10 cm^{-1}/GPa in the 0–7 GPa range (Table I). There is no noticeable difference between the absolute-frequency pressure shifts in bending and stretching modes, which makes the relative variation for the bending modes larger than for the stretching modes. This behavior is clearly reflected by the Grüneisen parameter of each mode: $\gamma = 1.6$ and 1.4 for the E and T_2 bending modes, respectively, while $\gamma(A_1) = 0.4$ and $\gamma(T_2) = 0.6$ for the stretching modes. Although γ values seem lower than expected for stretching modes ($\gamma \approx 1$–2) [36], it is a direct consequence of the larger bulk compressibility of Cs_2CoCl_4 with respect to the local compressibility of the $CoCl_4$ tetrahedron. As we will show in Sec. III C, local Grüneisen parameters of 1.6 and 2.4 are obtained for A_1 and T_2 stretching modes, respectively, if we use the local bulk modulus of the $CoCl_4$ instead of the crystal bulk modulus (Table I). This result is worthy for establishing structural correlations between bulk and local compressibilities from Raman spectroscopy, provided that we know the corresponding local Grüneisen parameter. The structural study reported here by XAS and XRD (Sec. III C) is essential to achieve this goal.

The Raman spectrum changes above 7 GPa, in agreement with the pressure-induced structural phase transition of Cs_2CoCl_4 observed at 7 GPa from optical absorption. The spectrum is poorly resolved, probably due to domain formation, stress induced along with the phase transition, or partial amorphization, and consistently with observations in other experiments (see below). However, there are three peaks above 250 cm^{-1} and two main peaks around 200 cm^{-1} which are not consistent with the presence of $CoCl_4$ tetrahedra but $CoCl_6$

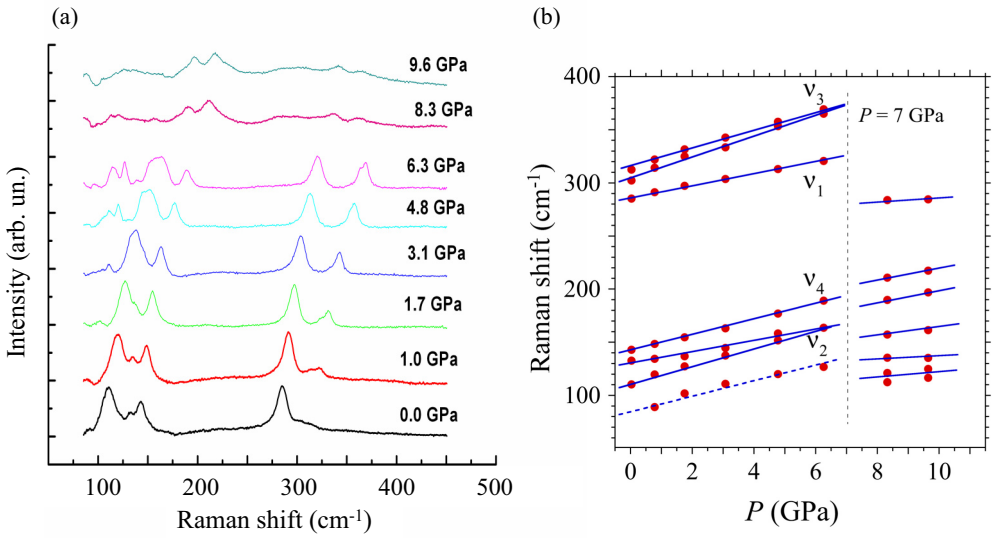

FIG. 6. (a) Pressure dependence of the Raman spectrum of Cs_2CoCl_4. (b) Pressure rates for each peak and corresponding Grüneisen parameters are given in Table I. Note the pressure-induced phase transition at 7 GPa.

octahedra. In particular, the high-pressure Raman spectrum looks similar to those expected on the basis of face- or edge-sharing $CoCl_6$ structures like those attained in $CsCoCl_3$ [37] or the related Li_2CoCl_4 [38] and Na_2MnCl_4 [39,40]. The Co-Co coupling provided by these edge- and face-sharing structures is completely different to that found in perovskite layers of corner-sharing $CoCl_6$ octahedra like Rb_2CoF_4 [41] or Rb_2MnCl_4 [42]. Although all these structures are compatible with sixfold coordinated Co^{2+}, the superexchange pathway between neighboring Co^{2+} ions is different in the case of corner-sharing and edge-sharing structures, and thus has a profound influence in the optical spectra.

The question arising is whether Cs_2CoCl_4 compression induces a phase transition associated with a new structure providing such a Co-Co coupling or does it lead to crystal decomposition into simpler species: $CsCoCl_3 + CsCl$. However, the recovery of the low-pressure phase in downstroke suggests that stoichiometry is preserved in this system and rules out such a possibility. A pressure-induced decomposition was suggested for $[(CH_3)_4N]_2MnCl_4$ and $[(CH_3)_4N]_2MnBr_4$ under pressure by means of time-resolved spectroscopy [32]. The green emission and corresponding excitation spectra characteristic of MnX_4 tetrahedra (X: Cl or Br) transforms to red emission at high pressure, the excitation of which is similar to MnX_6 octahedra in the one-dimensional $[(CH_3)_4N]MnX_3$. Therefore, the structural resemblance between $[(CH_3)_4N]_2MnX_4$ compounds and Cs_2CoCl_4 suggests a similar scenario for both compounds, discarding sample decomposition in the latter. Moreover, XAS data indicate that a high-pressure structure associated with edge-sharing $CoCl_6$ octahedra, like in Na_2MnCl_4, is likely.

C. X-ray absorption and x-ray diffraction on Cs_2CoCl_4 as a function of pressure

Figure 7 shows the evolution of the XRD pattern of Cs_2CoCl_4 with pressure. At ambient pressure the XRD pattern corresponds to an orthorhombic structure (*Pnma* space group; $a = 9.720$ Å, $b = 7.313$ Å, $c = 12.822$ Å [22]). Diffraction patterns can be described with the same *Pnma* space group up to the phase transition at 7 GPa. Above this pressure, the XRD pattern changes abruptly and a significant broadening of all reflections is observed. Consistently with Raman spectroscopy, such a broadening may be due to domain formation, stress, or partial amorphization of the chloride in the high-pressure phase. This behavior is clearly confirmed by the change in the XRD two-dimensional images, from initially spotted Bragg circles due to texture and preferred orientation in the low-pressure phase to homogeneous Bragg circles in the high-pressure phase. This means that texture effects disappear because of the multidomain (or grain) structure providing a better random orientation of microcrystallites. Upon pressure

TABLE I. Experimental Raman frequency of the vibrational optical modes of Cs_2CoCl_4 at $T = 290$ K (Figs. 5 and 6). The lattice modes correspond to internal modes of $CoCl_4$ and are labeled with T_d symmetry irreducible representations. Their pressure shift rate as well as the corresponding Grüneisen parameter associated with the crystal volume (γ) and the tetrahedron volume (γ_{loc}) have been derived from the corresponding crystal and local bulk moduli (Fig. 10).

Raman modes	Bending Cl-Co-Cl modes		Stretching Co-Cl modes	
$CoCl_4^{2-}$	$\nu_2(E)$	$\nu_4(T_2)$	$\nu_1(A_1)$	$\nu_3(T_2)$
ν (cm^{-1}) at $P = 0$	112	142	287	315
$\partial\nu/\partial P$(cm^{-1}/GPa)	8.4	7.4	5.5	9.8
$\gamma = (K_0/\nu)\partial\nu/\partial P$	1.6	1.1	0.4	0.6
$\gamma_{loc} = (K_{loc}/\nu)\partial\nu/\partial P$	6.2	4.3	1.6	2.4

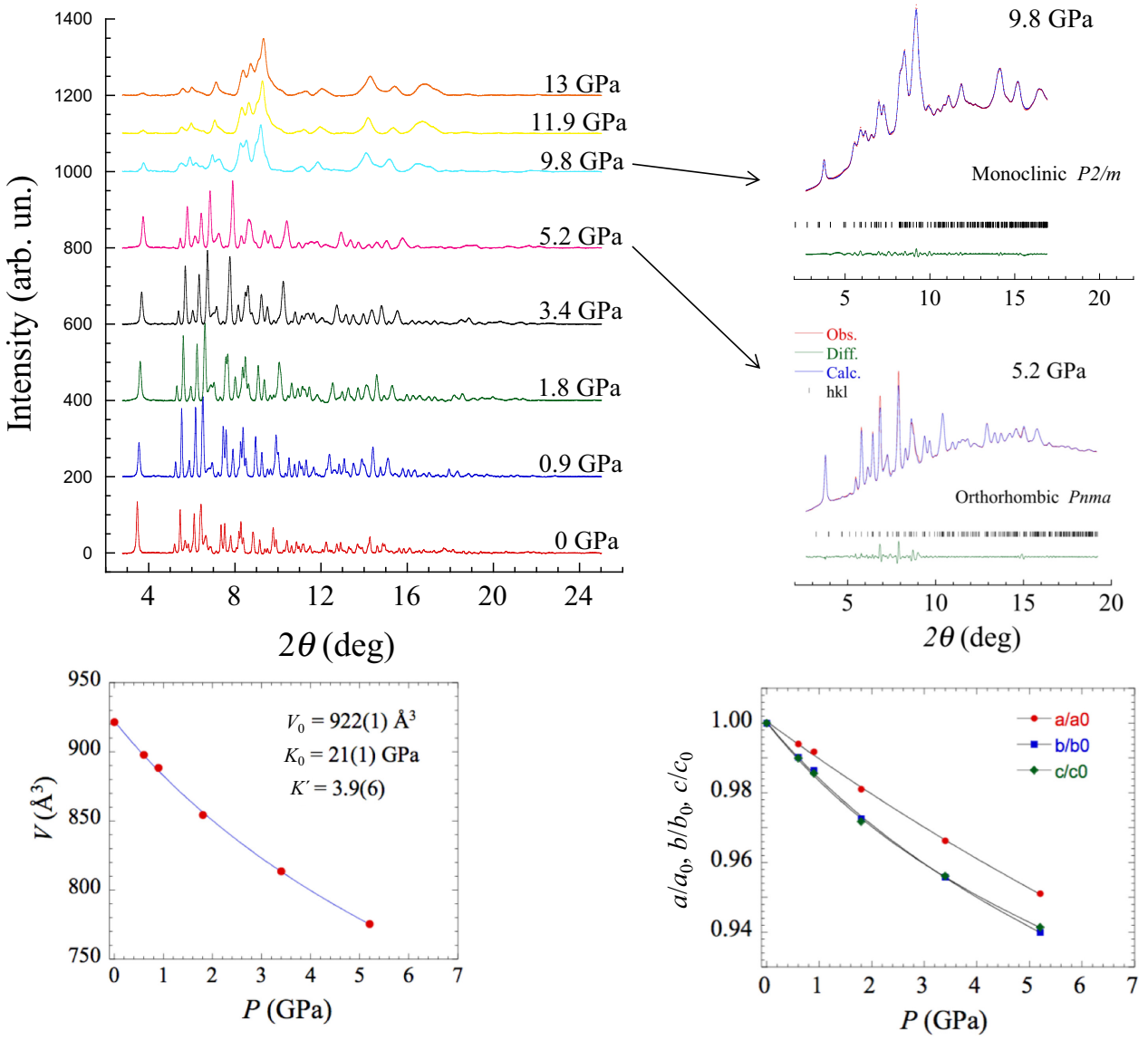

FIG. 7. Variation of XRD pattern of Cs_2CoCl_4 with pressure. Below 7 GPa, the low-pressure phase XRD diagram can be explained within an orthorhombic *Pnma* with lattice parameters $a = 9.259$ Å, $b = 6.912$ Å, and $c = 12.12$ Å at $P = 5.2$ GPa. The high-pressure phase has been indexed within a monoclinic $P2/m$ with $a = 8.611$ Å; $b = 11.051$ Å; $c = 3.834$ Å; and $\beta = 85.5°$ at $P = 9.8$ GPa. The variation $V(P)$ with the corresponding Murnaghan equation of state, and the relative variation of the lattice parameters in the *Pnma* phase are shown. The equation of state for each phase is shown in Fig. 10 (see Supplemental Material [54]).

release the low-pressure *Pnma* phase is recovered at nearly 2 GPa but maintains the homogeneous grain distribution.

The variation of the lattice parameters and crystal volume in the orthorhombic *Pnma* phase is represented in Fig. 7. Results are similar to those previously found for Cs_2CoCl_4 in the 0–5 GPa range [7]. The higher compression of the crystal along the *b* and *c* axis is noteworthy. Preferential compression along these directions favor packing of $CoCl_4$ tetrahedra by sharing two or more Cl^- ions. So, the structural variation under pressure in the *Pnma* phase foresees an evolution toward a chainlike structure either by edge- or face-sharing octahedra, as suggested from optical absorption and Raman data. The reversibility of the phase transformation suggests that the former structure is more likely.

The poor quality of the diffraction intensity pattern due to both texture and preferential orientation does not permit an unambiguous determination of the crystal structure, and thus of the internal coordinates associated with the Cl^- atoms. However, XAS experiments performed under high-pressure conditions allowed us to get the variation of the Co-Cl distance ($R_{Co\text{-}Cl}$) with pressure (Figs. 8–10). Nevertheless, we have described the XRD diffraction patterns above 7 GPa on the basis of a monoclinic $P2/m$ space group, which is a subgroup of the parent orthorhombic *Cmmm* and *Pbam* edge-sharing-type structures of Li_2CoCl_4 [38] and Na_2MnCl_4 [39,40], respectively. The pressure dependences of volume per Co in both phases are given together with variations of $R_{Co\text{-}Cl}$ in Fig. 10 (see Sec. IIID). It must be noted that the ambient pressure volume of the high-pressure $P2/m$ phase, 205 $Å^3$/Co, which is used as a fixed parameter in the EOS (equation of state) for such a phase, is determined from structural correlations of isomorphous structures containing

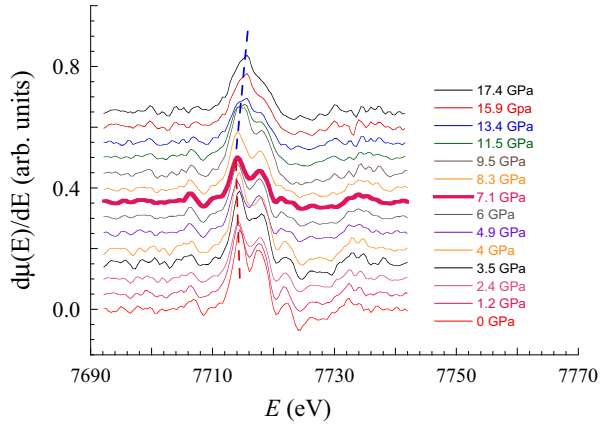

FIG. 8. Pressure dependence of the XANES first derivative corresponding to the Co K edge in Cs_2CoCl_4. The split peak at 7715 eV slightly shifts to lower energy with pressure in the *Pnma* low-pressure phase. It abruptly changes at $P_C = 7$ GPa and shifts to higher energy in the high-pressure phase. Note that the splitting progressively reduces with pressure.

isolated MCl_4 tetrahedra and MCl_6 edge-sharing octahedra. The volume per M ion in the Na_2MCl_4 structures is 177 and 178 Å^3 for tetrahedral $M =$ Zn [43] and Co [44], respectively, whereas it is of 155 and 159 Å^3 for octahedral $M =$ Fe [45] and Mn [40], respectively. It means a reduction of 89% on passing from a tetrahedron to an octahedron structure. A similar volume reduction is attained on passing from tetrahedral Li_2ZnCl_4(145 Å^3) [46] to octahedral Li_2CoCl_4 (133 Å^3) [38]. Therefore, we assume a similar volume reduction on passing from *Pnma* Cs_2CoCl_4 (measured 230.5 Å^3) to $P2/m$ Cs_2CoCl_4 (estimated 205 Å^3) at ambient pressure.

The $V(P)$ pressure dependence has been described by a Rydberg-Vinet EOS [47],

$$P(V) = 3K_0\eta^{\frac{-2}{3}}(1-\eta^{\frac{1}{3}})\exp\left[\frac{3}{2}(K'-1)(1-\eta^{\frac{1}{3}})\right], \quad \eta = \frac{V}{V_0},$$

with $V_0 = 230.5$ Å^3/Co, $K_0 = 21$ GPa, and $K' = 4.4$ in the *Pnma* low-pressure phase, and $V_0 = 205$ Å^3/Co (fixed value), $K_0 = 55$ GPa, and $K' = 4.3$ in the high-pressure $P2/m$ phase (Fig. 10). We selected this EOS for describing both phases since it is better suited than the Murnaghan EOS for pressures higher than the bulk modulus.

D. Pressure-induced structural transformation: $CoCl_4 \leftrightarrow CoCl_6$

Figures 8 and 9 show the first-derivative XANES and the corresponding Fourier-transform (FT) EXAFS of Cs_2CoCl_4 as a function of pressure. A magnification of the first FT peak associated with first Cl^- shell of Co^{2+} is also shown in Fig. 9. Both XANES and EXAFS clearly unravel the structural phase transition at 7 GPa. The first-derivative peak of the Co K edge at 7715 eV (Fig. 8) experiences a linear shift to lower energies with pressure in the *Pnma* phase, whereas it abruptly changes to higher energies in the high-pressure $P2/m$ phase. A similar pressure behavior is observed for $R_{\text{Co-Cl}}$ derived from EXAFS. Interestingly, $R_{\text{Co-Cl}}$ undergoes an abrupt lengthening at the phase transition pressure [Fig. 9(b)], suggesting that the phase transition involves a change of the Co^{2+} coordination from $CoCl_4(T_d)$ to $CoCl_6(O_h)$. The sharp increase of $R_{\text{Co-Cl}}$ from 2.17 to 2.27 Å at 7 GPa supports it. Moreover, the increase $\delta R_{\text{Co-Cl}} = 0.1$ Å is consistent with the proposed structural scenario, where $CoCl_6$ octahedra share common edges in the high-pressure phase similarly to Na_2MnCl_4 (or the similarly related Li_2CoCl_4) [38] rather than corners like in the layered perovskite Rb_2MnCl_4 [42]. Owing to this, Mn^{2+} chlorides provide a polytype variety to check variations of $R_{\text{Mn-Cl}}$ on passing from $MnCl_4$ tetrahedra ($R_{\text{Mn-Cl}} = 2.35$ Å in Cs_3MnCl_5 [48] or 2.34 Å in $[(CH_3)_4N]_2MnCl_4$ [25]) to different $MnCl_6$ packing structures: face sharing ($R_{\text{Mn-Cl}} =$ 2.55 Å in $MnCl_2$ [49]; 2.56 Å in $[(CH_3)_4N]MnCl_3$ [35,50]; 2.54 Å in $CsMnCl_3$ [51]), edge sharing ($R_{\text{Mn-Cl}} = 2.56$ Å in Na_2MnCl_4 [39,40]), and corner sharing ($R_{\text{Mn-Cl}} = 2.52$ Å in Rb_2MnCl_4 [42]; 2.48 Å in $RbMnCl_3$ [42]). The coordination change from $MnCl_4$ to $MnCl_6$ involves $\delta R_{\text{Mn-Cl}} = 0.2$ Å for face-sharing and edge–sharing structures, while $\delta R_{\text{Mn-Cl}} =$ 0.15 Å for corner-sharing structures at ambient pressure. Taking into account the variations of $R_{\text{Co-Cl}}$ with pressure in tetrahedral and octahedral coordinations as -0.01Å/GPa for $(Co,Mn)Cl_4$ and -0.02 Å/GPa for $(Co,Mn)Cl_6$ [1,5,32,35,44],

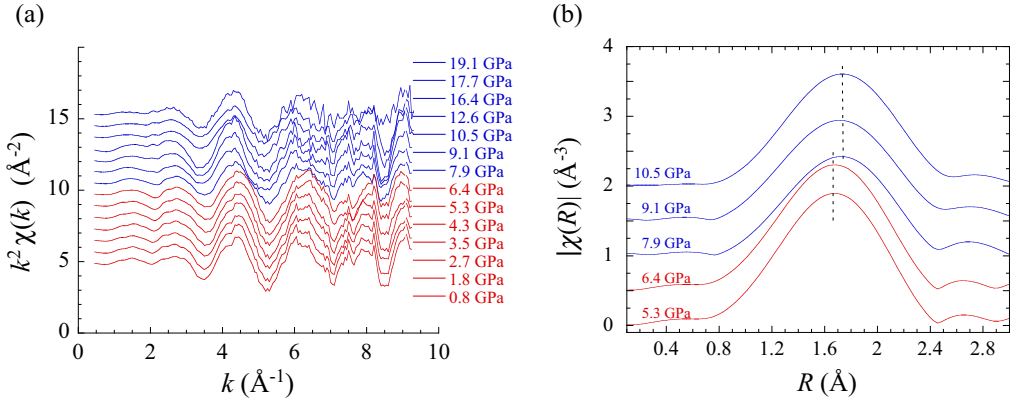

FIG. 9. (a) Pressure dependence of the EXAFS spectrum around the Co K edge in Cs_2CoCl_4 after background subtraction. (b) Variation of the EXAFS Fourier transform with pressure around the phase transition pressure, $P_C = 7$ GPa. The FT peak corresponds to scattering from the first Cl^- shell. Note that the associated R maximum abruptly shifts towards longer distances at 7 GPa. This lengthening is associated with an increase of the Co^{2+} coordination number of the first Cl^- shell at the phase transition

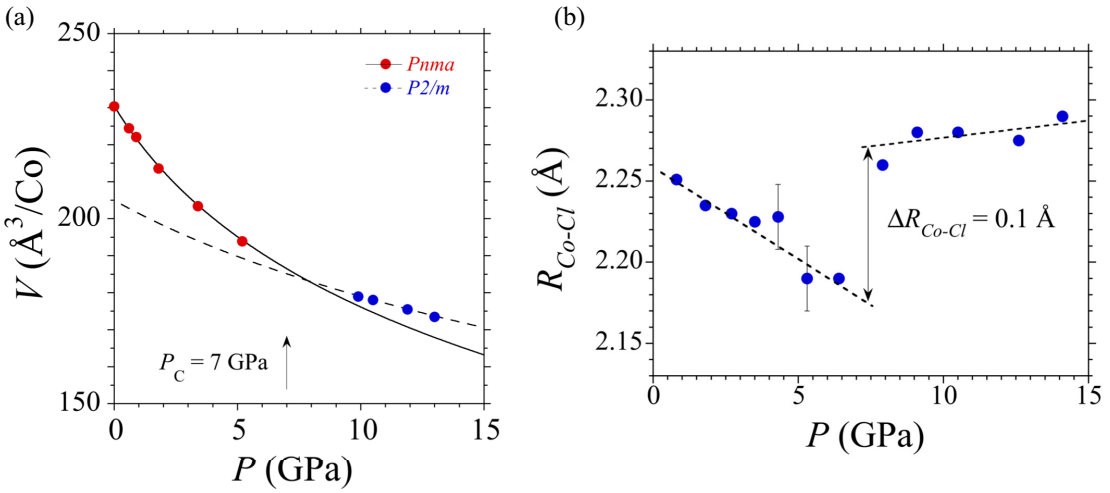

FIG. 10. (a) Pressure dependence of the Cs_2CoCl_4 volume per Co derived from XRD in the low-pressure *Pnma* and high-pressure $P2/m$ phases. The curves correspond to the fit of the experimental $V(P)$ data to a Rydberg-Vinet equation of state, with $V_0 = 230.5$ Å^3/Co, $K_0 = 21$ GPa, and $K' = 4.4$ in the *Pnma* low-pressure phase, and $V_0 = 205$ Å^3/Co (fixed value), $K_0 = 55$ GPa, and $K' = 4.3$ in the high-pressure $P2/m$ phase (see Supplemental Material [54]). (b) Pressure dependence of the Co-Cl bond distance $R_{\text{Co-Cl}}$ as derived from EXAFS. Note the abrupt increase of +0.1 Å in $R_{\text{Co-Cl}}$ with increasing pressure at the phase transition pressure, $P_C = 7$ GPa. The straight line in the low-pressure *Pnma* phase corresponds to the linear fit: $R_{\text{Co-Cl}} = 2.26 - 9.1\times10^{-3}P$ (in Å and GPa units). The associated local bulk modulus of the $CoCl_4$ tetrahedron is $K_{\text{loc}} = 83$ GPa.

we conclude that the jump of $R_{\text{Co-Cl}}$ associated with the change of coordination would decrease with respect to ambient conditions at a rate of −0.01Å/GPa. Therefore the measured jump $\delta R_{\text{Co-Cl}} = +0.1$ Å at 7 GPa is consistent with the proposed model of edge-sharing octahedra.

The changes experienced by the absorption spectrum at 7 GPa can also be explained according to the model. The high-pressure spectrum ($P > 7$ GPa) looks like the $ACoCl_3$(A = Rb,Cs) absorption spectrum [31], where the intense peaks appearing in the 1.5–2.5 eV range are assigned to d^7-intraconfiguration crystal-field transitions: $^4T_1(F) \rightarrow {}^4T_1(P)$ at $E_1 = 1.85$ eV; $^4T_1(F) \rightarrow {}^2A_1(G)+{}^2T_1(H)$ at $E_2 = 2.07$ eV, and $E_3 = 2.17$ eV, respectively; as well as a weak band at 2.45 eV probably related to the $^4T_1(F) \rightarrow {}^4A_1(F)$. The latter band experiences the largest blueshift with pressure, since it involves two electron excitations from t_{2g} to e_g orbitals: $t_{2g}{}^5\, e_g{}^2(^4T_1) \rightarrow t_{2g}{}^3\, e_g{}^4(^4A_1)$ [27]. The unexpected high intensity of the spin-forbidden transitions $^4T_1(F) \rightarrow {}^2A_1(G) + {}^2T_1(H)$ is noteworthy. The electric-dipole transition mechanism is mediated by both the exchange coupling mechanism and spin-orbit interaction coupling with the $^4T_1(P)$ state [31]. In a side comparison with $CsCoCl_3$ [31], the peak assignment is definitely clarified through their pressure shifts according to the TS diagram. The calculated slopes $(\frac{\partial E_i}{\partial P})$ $(i = 1\text{–}3)$ indicate that peak shift is first governed by reduction of Racah parameters B and C and second by an increase of Δ due to $R_{\text{Co-Cl}}$ shortening. In general, pressure-induced shifts can be described in terms of B, C, and Δ through the following equation:

$$\left(\frac{\partial E_i}{\partial P}\right)_{P_0} = \left(\frac{\partial E_i}{\partial B}\right)\frac{\partial B}{\partial P} + \left(\frac{\partial E_i}{\partial C}\right)\frac{\partial C}{\partial P} + \left(\frac{\partial E_i}{\partial \Delta}\right)\frac{\partial \Delta}{\partial P} = [A_i + (C/B)D_i]\frac{\partial B}{\partial P} + \left(\frac{\partial E_i}{\partial \Delta}\right)\frac{\partial \Delta}{\partial P} \quad (1)$$

For given C/B and Δ/B values at P_0, A_i and D_i depend on B for E_i, and i stands for the three peak energies, $i =$ 1–3 [26,27]. Quantitative estimates of these two effects can be obtained from the experimental peak shifts and calculated slopes $\frac{\partial E_i}{\partial \Delta}$ and $\frac{\partial E_i}{\partial B}$ $(i = 1\text{–}3)$ from the TS diagram (d^7). We know that the $^2T_1(H)$ energy (E_3) practically does not depend on Δ but on $B(\frac{\partial E_3}{\partial \Delta} = 0)$. This means that its pressure dependence can be written for $C/B = 4.4$ as (Table II)

$$\frac{\partial E_3}{\partial P} = 25\frac{\partial B}{\partial P} \quad (2)$$

TABLE II. Experimental pressure derivatives of the absorption peak energy, $\frac{\partial E_i}{\partial P}$ $(i = 1\text{–}3)$ for $Co^{2+}(O_h)$ in Cs_2CoCl_4 in the 7–20-GPa range (Fig. 4). Calculated pressure derivatives $\frac{\partial E_i}{\partial \Delta}$ and $\frac{\partial E_i}{\partial B}$ derived from the Tanabe-Sugano diagrams of Fig. 3. Crystal-field parameters of Co^{2+} $[d^7(O_h)]$ in Cs_2CoCl_4 at 7 GPa and their pressure derivative are also included.

	Energy pressure derivative[a]	
Experimental	$\partial E_1/\partial P = 7$ $\partial E_2/\partial P = 15$ $\partial E_3/\partial P = -10$	
Calculated slopes from Tanabe-Sugano diagram[b]	$\partial E_1/\partial \Delta = 0.8$ $\partial E_2/\partial \Delta = 0.9$ $\partial E_3/\partial \Delta = 0.0$	$\partial E_1/\partial B = 21.4$ $\partial E_2/\partial B = 29.4$ $\partial E_3/\partial B = 25.0$
Crystal-field parameters and pressure derivatives[c]	$B = 86$ meV $\partial B/\partial P = -0.4$	$\Delta = 750$ meV $\partial \Delta/\partial P = 20$

[a]Units in meV/GPa.
[b]$C/B = 4.4$ and $\Delta/B = 8.7$ for $d^7(O_h)$.
[c]Crystal-field parameters and their pressure derivative derived from the experimental energies at 7 GPa and their pressure shift rate in the 7–20 GPa range.

However, both $^4T_1(P)$ and $^2A_1(G)$ energies (E_1 and E_2, respectively) depend on B and Δ. Their slope from the TS diagram is also collected in Table II. Then Eq. (1) can be expressed for each transition as

$$\frac{\partial E_1}{\partial P} = \left(\frac{\partial E_1}{\partial B}\right)_{\Delta}\frac{\partial B}{\partial P} + \left(\frac{\partial E_1}{\partial \Delta}\right)_{B,C}\frac{\partial \Delta}{\partial P} \approx 21.4\frac{\partial B}{\partial P} + 0.8\frac{\partial \Delta}{\partial P}, \quad (3)$$

$$\frac{\partial E_2}{\partial P} = \left(\frac{\partial E_2}{\partial B}\right)_{\Delta}\frac{\partial B}{\partial P} + \left(\frac{\partial E_2}{\partial \Delta}\right)_{B,C}\frac{\partial \Delta}{\partial P} \approx 29.4\frac{\partial B}{\partial P} + 0.9\frac{\partial \Delta}{\partial P}. \quad (4)$$

From the measured $\frac{\partial E_i}{\partial P}$ coefficients given in Table II, we obtain $\frac{\partial B}{\partial P} = -0.4$ meV/GPa and $\frac{\partial \Delta}{\partial P} = +20(4)$ meV/GPa for Cs_2CoCl_4 in its high-pressure phase. These values compare with those obtained in the low-pressure phase for $CoCl_4$: $\frac{\partial B}{\partial P} = -0.92$ meV/GPa and $\frac{\partial \Delta}{\partial P} = +9.0$meV/GPa . The experimental values of B and Δ as well as their pressure derivatives for $CoCl_4$ (low-pressure phase) and $CoCl_6$ (high-pressure phase) in Cs_2CoCl_4 are consistent with the different crystal-field and Co-Cl covalency attained in T_d and O_h coordinations. While $\frac{\partial \Delta}{\partial P}$ for T_d is about half that for O_h, $\frac{\partial B}{\partial P}$ for T_d is twice as high as for O_h. These results fairly agree with those measured in other transition-metal chloride systems as $MnCl_6$ (O_h) in NH_4MnCl_3: $\frac{\partial B}{\partial P} = -0.3$ meV/GPa and $\frac{\partial \Delta}{\partial P} = +35$ meV/GPa [26,29,52], and in $MnCl_2$, $\frac{\partial B}{\partial P} = -0.3$ meV/GPa; $\frac{\partial \Delta}{\partial P} = +32$ meV/GPa) [1,53]. In $Cs_2ZnX_4 : Co^{2+}$ (*Pnma* phase) where the Co^{2+} occupies the substitutional Zn^{2+} site (T_d) as $CoCl_4$, these variations are $\frac{\partial B}{\partial P} = -0.7$ meV/GPa, and $\frac{\partial \Delta}{\partial P} = 9$ meV/GPa [5], and are similar to those found in $MnCl_4$ in $[(CH_3)_4N]_2MnCl_4$, $\frac{\partial B}{\partial P} = -0.35$ meV/GPa; $\frac{\partial \Delta}{\partial P} = +8$ meV/GPa [32].

Interestingly, the knowledge of $\frac{\partial \Delta}{\partial P}$ and $\frac{\partial R_{\text{Co-Cl}}}{\partial P}$ in Cs_2CoCl_4 (*Pnma* phase) allows us to know the $R_{\text{Co-Cl}}$-dependence of B and Δ. On the assumption of a R dependence of Δ as R^{-n}, we can obtain the exponent n from the experimental variations through the following equation:

$$\frac{1}{\Delta_0}\frac{\partial \Delta}{\partial P} = \frac{-n}{R_{\text{Co-Cl}}}\frac{\partial R_{\text{Co-Cl}}}{\partial P}. \quad (5)$$

Taking $\Delta_0 = 0.42$ eV and $R_{\text{Co-Cl}} = 2.26$ Å [22], we obtain

$$n = -\frac{R_{\text{Co-Cl}}}{\Delta_0}\frac{\frac{\partial \Delta}{\partial P}}{\frac{\partial R_{\text{Co-Cl}}}{\partial P}} = -\frac{2.26}{420} \times \frac{9}{-0.01} = 4.8 \approx 5. \quad (6)$$

The exponent of the variation is similar to that provided by crystal-field theory and *ab-initio* calculations, and is also derived experimentally in an ample variety of O_h transition-metal halides and oxides [1]. The experimental determination of n for $CoCl_4$ (T_d) in Cs_2CoCl_4 is noteworthy since there is a lack of structural data dealing with such correlation in T_d systems [32,35]. Furthermore, it provides a means of complementing R dependences of the crystal-field strength in other coordination geometries besides O_h, which is important in order to establish correlations between local bond distances in $MX_4{}^{2-}$ systems from optical spectroscopy. Additionally, we have determined the local Grüneisen parameters associated with the vibrational modes of T_d $CoCl_4$ (Table I) as a complementary tool to establish structural correlations through Raman spectroscopy.

IV. CONCLUSIONS

From the pressure dependence of the XRD, XAS, Raman scattering, and electronic absorption of Cs_2CoCl_4 we show that the electronic and vibrational structures can be explained to a great extent on the basis of T_d $CoCl_4$, the volume of which is 4 times more incompressible than Cs_2CoCl_4 bulk. In particular, the totally symmetric vibrational mode frequency (A_1) and crystal-field strength (Δ) scale with $R_{\text{Co-Cl}}$ as $R_{\text{Co-Cl}}^{-3\gamma_{loc}}$ and $R_{\text{Co-Cl}}^{-n}$, respectively, having a Grüneisen parameter, $\gamma_{\text{loc}} = 1.6$ and an exponent $n = 4.8$, thus enabling to get $R_{\text{Co-Cl}}$ from either the Raman frequency $\nu(A_1)$ or the crystal-field splitting Δ. The piezochromic phase transition at 7 GPa yields an increase of Co^{2+} coordination number from $4(T_d)$ to $6(O_h)$ with a $R_{\text{Co-Cl}}$ lengthening of $+0.1$ Å. The electronic absorption, Raman spectra, and XAS indicate that the $CoCl_6$ octahedra in the high-pressure phase share common edges similarly to Na_2MnCl_4 (*Pbam*) and rule out the Cs_2CoCl_4 decomposition into $CsCl + CsCoCl_3$. XRD patterns can be described in terms of a partially amorphized single phase with monoclinic $P2/m$ space group, which can be related to the Na_2MnCl_4 *Pbam*. The piezochromism is associated with the strong decrease of the absorption bands around 500–600 nm (2–2.5 eV) due to the change in inversion center at Co^{2+} on passing from T_d to O_h (or D_{3d}). The weaker absorption in the high-pressure phase is caused by the spin-effective mechanism, which is very efficient in exchange coupled systems having Cl^--edge or Cl^--face-sharing Co-Co pathways.

ACKNOWLEDGMENTS

Financial support from the Spanish Ministerio de Economía y Competitividad (Project No. MAT2015-69508-P) and MALTA-CONSOLIDER (Ref. No. MAT2015-71070-REDC) is acknowledged. We also acknowledge financial support and facilities from the Synchrotron SOLEIL (Proposal Ref. No. 20100989) and Synchrotron DIAMOND (Project Ref. No. EE1655). I.H. thanks the EU FP7 for his Marie Curie CIG grant (Grant No. MC-CIG 303535).

[1] H. G. Drickamer and C. W. Frank, *Electronic Structure, Electronic Transitions and the High Pressure Chemistry and Physics of Solids* (Chapman and Hall, London, 1973).

[2] K. V. Yumasev, Appl. Opt. **38**, 6343 (1999).

[3] G. Karlsson, V. Pasiskevicius, F. Laurell, J. A. Tellefsen, B. Denker, B. I. Galagan, V. V. Osiko, and S. Sverchkov, Appl. Opt. **39**, 6188 (2000).

[4] M. Kenzelmann, R. Coldea, D. A. Tennant, D. Visser, M. Hofmann, P. Smeibidl, and Z. Tylczynski, Phys. Rev. B **65**, 144432 (2002).

[5] D. R. Stephens and H. G. Drickamer, J. Chem. Phys. **35**, 429 (1961).

[6] B. N. Figgis, M. Gerloch, and R. Mason, Proc. R. Soc. London, Ser. A **279**, 210 (1964).

[7] Y. Xu, S. Carlson, K. Söderberg, and R. Norrestam, J. Solid State Chem. **153**, 212 (2000).

[8] D. Machon, A. Grzechnik, and K. Friese, J. Phys.: Condens. Matter **21**, 405405 (2009).

[9] Ü. Özgür, Ya. I. Alivov, C. Liu, A. Teke, M. A. Reshchikov, S. Doğan, V. Avrutin, S.-J. Cho, and H. Morkoç, J. Appl. Phys. **98**, 041301 (2005), and references therein.

[10] H. A. Weakliem and D. S. McClure, J. Appl. Phys. **33**, 347 (1962).

[11] P. Koidl, Phys. Rev. B **15**, 2493 (1977).

[12] C. Renero-Lecuna, R. Martín-Rodríguez, J. A. González, F. Rodríguez, G. Almonacid, A. Segura, V. Muñoz-Sanjosé, D. R. Gamelin, and R. Valiente, Chem. Mater. **26**, 1100 (2013).

[13] N. V. Kuleshov, V. P. Mikhailov, V. G. Scherbitsky, P. V. Prokoshin, and K. V. Yumashev, J. Lumin. **55**, 265 (1993).

[14] L. Nataf, F. Rodríguez, R. Valiente, and V. Ulanov, J. Lumin. **129**, 1602 (2009).

[15] J. Ferguson, D. L. Wood, and L. G. Van Uitert, J. Chem. Phys. **51**, 2904 (1969).

[16] O. P. Lamba and S. K. Sinha, Solid State Commun. **57**, 365 (1986).

[17] I. Noiret, Y. Guinet, and A. Hedoux, Phys. Rev. B **52**, 13206 (1995).

[18] H. Soling, Acta Chem. Scand. **22**, 2793 (1968).

[19] J. Ferguson, D. L. Wood, and K. Knox, J. Chem. Phys. **39**, 881 (1963).

[20] J. P. Boucher, G. Rius, and Y. Henry, Europhys. Lett. **4**, 1073 (1987).

[21] I. Mogi, M. Takeda, G. Kido, Y. Nakagawa, H. Kikuchi, and Y. Ajiro, J. Phys. Soc. Jpn. **58**, 2188 (1989).

[22] B. N. Figgis, P. A. Reynolds, and A. H. White, J. Chem. Soc. (Dalton Trans.) **7**, 1737 (1987).

[23] S. Klotz, J. C. Chervin, P. Munsch, and G. Le Marchand, J. Phys. D: Appl. Phys. **42**, 075413 (2009).

[24] A. Moral and F. Rodriguez, Rev. Sci. Instrum. **66**, 5178 (1995).

[25] H. Mashiyama and N. Koshiji, Acta Crystallogr. B: Struct. Sci. **45**, 467 (1989).

[26] J. S. Griffith, *The Theory of Transition-Metal Ions* (Cambridge University Press, Cambridge, UK, 1980).

[27] S. Sugano, Y. Tanabe, and H. Kamimura, *Multiplets of Transition-Metal Ions* (Academic Press, New York, 1970).

[28] Y. Tanabe, T. Moriya, and S. Sugano, Phys. Rev. Lett. **15**, 1023 (1965).

[29] F. Rodriguez, D. Hernandez, and H. U. Güdel, Phys. Rev. B **60**, 10598 (1999).

[30] U. Kambli and H. U. Güdel, J. Phys. C: Solid State Phys. **17**, 4041 (1984).

[31] C. F. Putnik and S. L. Holt, Inorg. Chem. **16**, 1010 (1977).

[32] Y. Rodríguez-Lazcano, L. Nataf, and F. Rodríguez, Phys. Rev. B **80**, 085115 (2009).

[33] J. Henocque1, A. Hedoux, and J. L. Sauvajol, J. Raman Spect. **24**, 371 (1993).

[34] V. I. Torgashev, Yu. I. Yuzyuk, L. M. Rabkin, and Yu. I. Durnev, Phys. Stat. Sol. (b) **167**, 321 (1991).

[35] J. A. Barreda-Argüeso, L. Nataf, Y. Rodríguez-Lazcano, F. Aguado, J. González, R. Valiente, F. Rodríguez, H. Wilhelm, and A. P. Jephcoat, Inorg. Chem. **53**, 10708 (2014).

[36] F. Decremps, J. Pellicer-Porres, A. M. Saitta, J. C. Chervin, and A. Polian, Phys. Rev. B **65**, 092101 (2002).

[37] W. P. Lehmann, W. Breitling, and R. Weber, J. Phys. C: Solid State Phys. **14**, 4655 (1981).

[38] M. Schneider, H. D. Lutz, and J. K. Cockcroft, Z. Kristallogr. **203**, 183 (1993).

[39] H. D. Lutz, K. Wussow, and P. Kuske, Z. Naturforsch. **42b**, 1379 (1987).

[40] H. J. Seifert, F. W. Koknat, and Z. Anorg. Allg. J. Chem. **341**, 269 (1965).

[41] M. Welsch and D. Babel, Z. Naturforsch. **46b**, 161 (1991).

[42] J. Goodyear, E. M. Ali, and G. A. Steigmann, Acta Crystallogr. B **33**, 2932 (1977).

[43] Z. Zhang and H. D. Lutz, Z. Kristallogr. **210**, 691 (1995).

[44] C. J. J. Van Loon and D. Visser, Acta Cryst. B **33**, 188 (1977).

[45] C. J. J. Van Loon and D. Visser, Acta Cryst. B **31**, 770 (1975).

[46] M. Sassmannshausen, I. Solinas, and H. D. Lutz, Z. Kristallogr. **211**, 819 (1996).

[47] P. Vinet, J. Ferrante, J. H. Rose, and J. R. Smith, J. Geophys. Res. **92**, 9319 (1987).

[48] P. A. Reynolds, B. N. Figgis, and A. H. White, Acta Crystallogr. B **37**, 508 (1981).

[49] A. Ferrari, A. Braibanti, and G. Bigliardi, Acta Crystallogr. **16**, 846 (1963).

[50] K. Hasebe and T. Asahi, Acta Crystallogr. C: Cryst. Struct. Commun. **45**, 841 (1989).

[51] T. I. Li, G. D. Stucky, and G. L. McPherson, Acta Crystallogr. B **29**, 1330 (1973).

[52] D. Hernández, F. Rodríguez, M. Moreno, and H. U. Güdel, Physica B **265**, 186 (1999).

[53] J. C. Zahner and H. G. Drickamer, J. Chem. Phys. **35**, 1483 (1961).

[54] See Supplemental Material at http://link.aps.org/supplemental/10.1103/PhysRevB.95.014110 for structural data from x-ray diffraction.